

UNBIASED GRADIENT ESTIMATION FOR EVENT BINNING VIA FUNCTIONAL BACKPROPAGATION

Jinze Chen, Wei Zhai*, Han Han, Tiankai Ma, Yang Cao, Bin Li, Zheng-Jun Zha

MoE Key Laboratory of Brain-inspired Intelligent Perception and Cognition,

University of Science and Technology of China

{chjz@mail.,wzhai056@,hanh@mail.,tiankaima@mail.}ustc.edu.cn

{forrest,binli,zhazj}@ustc.edu.cn

ABSTRACT

Event-based vision encodes dynamic scenes as asynchronous spatio-temporal spikes called events. To leverage conventional image processing pipelines, events are typically binned into frames. However, binning functions are discontinuous, which truncates gradients at the frame level and forces most event-based algorithms to rely solely on frame-based features. Attempts to directly learn from raw events avoid this restriction but instead suffer from biased gradient estimation due to the discontinuities of the binning operation, ultimately limiting their learning efficiency. To address this challenge, we propose a novel framework for unbiased gradient estimation of arbitrary binning functions by synthesizing weak derivatives during backpropagation while keeping the forward output unchanged. The key idea is to exploit integration by parts: lifting the target functions to functionals yields an integral form of the derivative of the binning function during backpropagation, where the cotangent function naturally arises. By reconstructing this cotangent function from the sampled cotangent vector, we compute weak derivatives that provably match long-range finite differences of both smooth and non-smooth targets. Experimentally, our method improves simple optimization-based egomotion estimation with 3.2% lower RMS error and $1.57\times$ faster convergence. On complex downstream tasks, we achieve 9.4% lower EPE in self-supervised optical flow, and 5.1% lower RMS error in SLAM, demonstrating broad benefits for event-based visual perception. Source code can be found at <https://github.com/chjz1024/EventFBP>.

1 INTRODUCTION

Event-based visual perception has recently emerged as a novel paradigm to encode highly dynamic scenes with spatio-temporal event spikes. This paradigm shift brings new opportunities to high-speed and low-latency visual information processing, such as fine-grained optical flow estimation (Zhu et al., 2018; Gehrig et al., 2021b; Shiba et al., 2023; Hamann et al., 2024; Luo et al., 2024; Wan et al., 2024; 2025; Han et al., 2025), high-speed robot localization (Vidal et al., 2018; Zhou et al., 2021; Hines et al., 2025), and blurless video generation (Pan et al., 2019; Rebecq et al., 2019; Tulyakov et al., 2021; Wu et al., 2024; Xu et al., 2025; Liao et al., 2025).

To leverage conventional image processing pipelines, a common practice is to apply data binning techniques to convert irregular events into dense frames (Gallego et al., 2020), as shown in Figure 1. However, binning functions are inherently discontinuous, which truncates gradients at the frame level and forces most event-based algorithms to rely solely on frame-based features. Existing approaches often resort to smooth binning to restore differentiability to raw events, but such surrogates inevitably introduce bias in the gradients, leading to suboptimal learning efficiency.

This challenge reflects a broader issue in learning with discontinuous nonlinearities in neuromorphic computing, where spiking neuron models introduce non-differentiable functions (Eshraghian et al., 2023). Existing solutions, such as surrogate gradients (Neftci et al., 2019) or straight-through estimators (Yin et al., 2019), provide heuristic gradients, but they lack unbiasedness guarantees.

*Correspondence to: Wei Zhai <wzhai056@ustc.edu.cn>

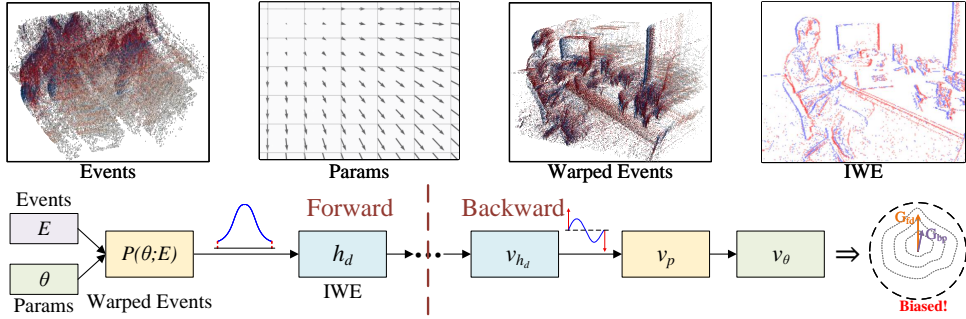


Figure 1: **Event binning and the gradient bias problem.** **Top:** Spatio-temporal event clouds (Events) are geometrically warped using motion parameters (Params) and aggregated into an Image of Warped Events (IWE) using a binning function. **Bottom Left (Forward):** The warping function $P(\theta; E)$ transforms input events E and parameters θ into warped coordinates. These are processed by a discontinuous binning function h_d to produce the IWE. **Bottom Right (Backward):** The adjoint (cotangent vector) of the IWE, denoted as v_{h_d} , is propagated back to update parameters. However, the discontinuity of h_d results in non-computable Dirac delta functions when computing the gradient v_p for the warped events. **Result:** The computed backpropagation gradient G_{bp} deviates from the true finite difference gradient G_{fd} , shown in the contour plot as a "Biased!" estimation.

From a mathematical perspective, weak derivatives (Kuttler, 2017) generalize classical derivatives to discontinuous functions. While their pointwise values may be non-computable (e.g., Dirac delta), their integrals are well-defined and can be computed via integration by parts. This observation is crucial: if we can computationally match the integral of weak derivatives, then the resulting gradient estimation recovers unbiasedness.

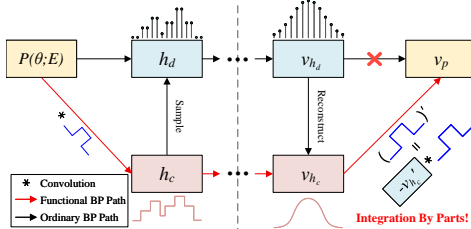


Figure 2: **The proposed Functional Backpropagation (FBP) framework.** To resolve discontinuities in the ordinary path (top, discrete binning h_d), we lift the operation to a functional space (bottom, continuous binning h_c). FBP bridges the two by reconstructing the continuous cotangent function v_{h_c} from the discrete samples v_{h_d} . Using integration by parts, we replace the undefined Dirac delta evaluation with a convolution (*) of v_{h_c} and the kernel derivative, synthesizing an unbiased gradient v_p .

To find such an integral, we dive into the backpropagation process and find that if we lift the binning function to the space of functionals, an integral of the respective gradient and the cotangent function naturally arises, which is provably sampled by the cotangent vector, as shown in Figure 2. Because cotangent functions naturally encode continuous motion flow, smooth priors can be utilized to reconstruct them from the cotangent vector irrespective of the forward pass. This allows us to derive an exact formula for the synthesized weak derivative of the binning function, which is provably shown to approximate long-range finite differences of arbitrary target functions. It also applies to continuous soft binning functions, where the synthesized gradients may help to skip local extremes.

To validate all the above claims, we first conduct analytical studies on simple tasks of event-based motion estimation, with an impressive result on the convergence speed and increased accuracy. We then conduct experiments on real-world tasks of optical-flow estimation and SLAM to show its wide applicability.

To summarize, our main contributions are:

1. We identify and formalize the fundamental issue of biased gradient estimation in event-based pipelines, stemming from the discontinuity of binning functions.
2. We propose a novel functional backpropagation framework that lifts binning functions into functional space, enabling gradient computation via weak derivatives. By applying integration by parts, our method avoids Dirac deltas and restores unbiasedness.

3. We derive an exact formula for the synthesized weak derivative, proving its equivalence to long-range finite differences for arbitrary functions, and show that it naturally generalizes to both discontinuous and smooth kernels.
4. We demonstrate consistent improvements across tasks: 3.7% lower RMS velocity error with $1.57\times$ faster convergence in controlled settings, 9.4% lower EPE in optical flow, and 5.1% lower RMS trajectory error in SLAM.

2 RELATED WORK

Binning in Event-Based Vision. In event-based vision, binning extends beyond its canonical form to support learning diverse visual representations. Two main types can be distinguished depending on where the information resides. The first focuses on binning weights, such as constants or event polarities (Maqueda et al., 2018; Luo et al., 2025), latest event timestamps (Lagorce et al., 2016; Ghosh & Gallego, 2025), or relative event intervals (Pan et al., 2019; Teng et al., 2022), which are primarily used to model irradiance change, motion, and gradients, respectively. These methods typically ignore binning gradients during learning and thus suffer from information loss. The second type focuses on binning locations, where events undergo parametric transformations, and parameters are recovered by optimizing sharpness metrics of the resulting event frames (Gallego et al., 2018; Gu et al., 2021; Shiba et al., 2024). While this approach captures complex spatio-temporal dynamics, it is fundamentally limited by the non-differentiability of the binning function. Our work is mainly concerned with this latter category.

Learning with Discontinuous Nonlinearities. There are three common approaches to restoring differentiability for discontinuous functions. The most direct is function relaxation (Huh & Sejnowski, 2018), but it alters the output and may compromise its physical meaning. Straight-through estimators (STE) (Yin et al., 2019) heuristically replace the gradient with a surrogate, while surrogate gradients (SG) (Neftci et al., 2019) introduce continuous relaxations of the true gradients. However, none of these methods guarantee unbiasedness, and their effectiveness often depends on domain expertise in choosing appropriate relaxations. Our method instead reconstructs a continuous relaxation of the cotangent function, providing a complementary alternative to surrogate gradients with the key property of unbiasedness.

Weak and Functional Derivatives. Our method draws on functional analysis, in particular weak derivatives and functional derivatives. Weak derivatives are defined through smooth test functions, where integration by parts provides an alternative characterization (Kuttler, 2017). Functional derivatives extend the notion of gradients to functionals, playing a central role in the calculus of variations (Frigyik et al., 2008). While these concepts are typically of theoretical interest due to computational intractability, we show that they naturally arise in backpropagation when lifting binning functions to the space of functionals, thereby enabling their practical use in learning.

3 METHODOLOGY

This section is organized in four parts: First, we extend ordinary backpropagation to functionals where an integral form naturally arises alongside the cotangent function, by deriving the chain rule for arbitrary functionals besides integrals encountered in the calculus of variations. Then we prove that an ordinary backpropagation pass samples the cotangent function with cotangent vectors, so that signal reconstruction techniques can be applied to compute the weak derivative of binning functions. Subsequently, we present a pseudocode implementation to bridge the gap between the theoretical derivation and practical application in forward and backward modes. Finally, we experimentally validate that the method approximates long-range finite differences for various loss functions, and the formal proof of unbiasedness is included in the appendix.

We start with a notational convention to distinguish between functionals and pointwise evaluation:

- Square brackets are used for functionals acting on elements of a function space; *e.g.*, $f[u]$.
- Parentheses are used for pointwise evaluation of ordinary functions; *e.g.*, $, g(x)$.

3.1 FUNCTIONAL BACKPROPAGATION

A *functional* is defined by a rule, which associates a number with a function. Let $\mathcal{H}(X) := (X \rightarrow \mathbb{R})$ represent the space of real-valued functions defined on X , then a *functional* f is defined as a mapping $u \in \mathcal{H}(X) \mapsto f[u]$, where $f[u]$ can itself be another function on space $\mathcal{H}(Y)$. In this definition, functionals can be chained and used to derive the chain rule.

Since functionals are functions that consume an entire function to give another function, their differentials are also functions. From the knowledge of the Fréchet derivative and the Riesz representation theorem in functional analysis, we have the following result:

Definition 1. Assuming f is a differentiable functional on vectors spaces from $\mathcal{H}(X)$ to $\mathcal{H}(Y)$, then the derivative of f at $u \in \mathcal{H}(X)$ is represented by the derivative kernel function $\frac{\delta f[u](y)}{\delta u(x)}$, which satisfies the limit:

$$\lim_{\|\delta u\| \rightarrow 0} \frac{\|f[u + \delta u] - f[u] - \int_X \frac{\delta f[u]}{\delta u(x)} \delta u(x) dx\|_{\mathcal{H}(Y)}}{\|\delta u\|_{\mathcal{H}(X)}} = 0. \quad (1)$$

With the above definition, the chain rule for functionals is described in terms of integrals.

Theorem 1. Let $\mathcal{H}(X) \xrightarrow{f} \mathcal{H}(Y) \xrightarrow{g} \mathcal{H}(Z)$ where f and g are differentiable functionals, then the composite functional $g \circ f$ is also differentiable and has the representation:

$$\frac{\delta g[f[u]](z)}{\delta u(x)} = \int_Y \frac{\delta g[f[u]](z)}{\delta f[u](y)} \frac{\delta f[u](y)}{\delta u(x)} dy. \quad (2)$$

When X, Y, Z are finite sets, Theorem 1 becomes the familiar chain rule $J_{g \circ f} = J_g \cdot J_f$ where J is the finite-dimensional Jacobian matrix, since integration becomes summation on finite sets. So any composable differentiable mappings have a chain rule, where every ordinary function induces a Jacobian-vector product and every functional induces an integral transform with the derivative kernel function.

To compute the Jacobians, classical backpropagation recursively computes $vJ_{g \circ f}$ using the associative property of matrix multiplication on Jacobians as $(vJ_g) \cdot J_f$, where $v \in \mathcal{H}(Z)$ is called a cotangent vector (Shi et al., 2024). The extension for infinite-dimensional functionals is a function $v(\cdot) \in \mathcal{H}(Z)$, and we call it the cotangent function. In analogy, we call the process of recursively computing the cotangent function using the chain rule **Functional Backpropagation (FBP)**.

3.2 SYNTHESIZING WEAK DERIVATIVES OF THE BINNING FUNCTION

An event-based algorithm accepts a group of events as input, defined as

$$\mathcal{E} = \{e_i = (t_i, x_i, y_i, p_i)\}_{i=1}^{N_e}, \quad (3)$$

where e_i represents an event with timestamp t_i , pixel location (x_i, y_i) , and polarity $p_i \in \{-1, +1\}$ representing sign of brightness change, and N_e is the number of events. A parametric transform maps \mathcal{E} to D-dimensional weighted points

$$\mathcal{P} = \{e'_i = (x'_{i1}, \dots, x'_{iD}, w'_i)\}_{i=1}^{N_e}, \quad (4)$$

where x'_{i_d} is the transformed location and w'_i is the weight. The binning function \mathbf{h} is a map from \mathcal{P} to $\mathbb{R}^{W_1 \times \dots \times W_D}$ where W_d is the number of bins. The value at index (j_1, \dots, j_D) is defined as

$$h_{j_1, \dots, j_D} = \sum_{i=1}^{N_e} w'_i \prod_{d=1}^D k_d \left(\frac{x'_{i_d} - j_d \Delta_d}{\Delta_d} \right), \quad (5)$$

where $k_d(\cdot)$ is the binning kernel with finite support and Δ_d is the binning width. This section provides an intuitive derivation of the formula for synthesizing the weak derivative $\frac{\partial h_{j_1, \dots, j_D}}{\partial x'_{i_d}}$. To simplify the derivation, our discussion is restricted to the $D = 1$ case, but the result can be easily extended to arbitrary dimensions. A structured Theorem-Proof is provided in the appendix.

We restate the definition of 1D event binning function \mathbf{h} with input points \mathcal{P} as:

$$\mathbf{h}(\mathcal{P}) = (h_1(\mathcal{P}), \dots, h_W(\mathcal{P})), \quad h_j(\mathcal{P}) = \sum_{i=1}^{N_e} w'_i k\left(\frac{x'_i - j\Delta}{\Delta}\right). \quad (6)$$

To learn the parameters, a scalar loss is constructed from the obtained $\mathbf{h}(\mathcal{P})$ using $f_d : \mathbf{h}(\mathcal{P}) \mapsto f_d[\mathbf{h}(\mathcal{P})] \in \mathbb{R}$. A continuous binning function $h(\mathcal{P}) \in \mathcal{H}(\mathbb{R})$ can be obtained by replacing $j\Delta$ with a continuous parameter x :

$$h[\mathcal{P}](x) = \sum_{i=1}^{N_e} w'_i k\left(\frac{x'_i - x}{\Delta}\right), \quad (7)$$

A natural mapping exists from $h[\mathcal{P}]$ to $\mathbf{h}[\mathcal{P}]$ using the sampling functional $\mathcal{S} : h[\mathcal{P}] \mapsto \mathcal{S}[h[\mathcal{P}]] := (h(\Delta), \dots, h(W\Delta)) = \mathbf{h}[\mathcal{P}]$. The sampling operator induces a functional $f_c := f_d \circ \mathcal{S}$.

We denote the space of discrete binning values as \mathcal{H}_d and the space of continuous binning values as \mathcal{H}_c , and represent their relationship using the following commutative diagram:

$$\begin{array}{ccccc} & & \mathcal{H}_c & & \\ & \nearrow h & \downarrow \mathcal{S} & \searrow f_c & \\ \mathcal{P} & \xrightarrow{\mathbf{h}} & \mathcal{H}_d & \xrightarrow{f_d} & \mathbb{R} \end{array} \quad (8)$$

To compute $\frac{\partial f_c}{\partial x'_i}$, functional backpropagation computes the cotangent vector $v_{x'_i}$ from v_f by:

$$v_h(x) = v_f \frac{\delta f_c}{\delta h(x)}, \quad v_{x'_i} = \int_{\mathbb{R}} v_h(x) \frac{\partial h(x)}{\partial x'_i} dx, \quad (9)$$

The cotangent function $v_h(\cdot)$ can also be computed during the normal backpropagation as $f_c = f_d \circ \mathcal{S}$. Using the chain rule, we have:

$$v_h(x) = \sum_{j=1}^W v_{h_j} \frac{\delta h_j}{\delta h(x)} = \sum_{j=1}^W v_{h_j} \delta(x - j\Delta), \quad (10)$$

where v_{h_j} is the classical cotangent vector of f_d during backward pass and $\delta(\cdot)$ is the Dirac delta. In signal processing terms, Equation (10) states that a normal backward pass of the binning function \mathbf{h} surrogates the cotangent function with a Dirac comb modulated by the cotangent vector. Fixing $W\Delta$, this surrogate becomes exact as $\Delta \rightarrow 0$, and at this time, we have:

$$\lim_{\Delta \rightarrow 0} \frac{1}{\Delta} v_{h_j} = v_h(j\Delta). \quad (11)$$

This result connects the cotangent function and cotangent vector by the sampling rule, so we can use normal signal reconstruction methods to reconstruct the cotangent function and derive an exact formula for $\frac{\partial f_c}{\partial x'_i}$. Since cotangent functions naturally encode smooth motion flow, one simple solution is to replace $\delta(\cdot)$ in Equation (10) with another kernel $\frac{1}{\Delta} l(\frac{\cdot}{\Delta})$, then we have:

$$\tilde{v}_{x'_i} = \sum_{j=1}^W \int_{\mathbb{R}} v_{h_j} \frac{w'_i}{\Delta^2} l'\left(\frac{x - j\Delta}{\Delta}\right) k\left(\frac{x'_i - x}{\Delta}\right) dx \stackrel{(a)}{=} \sum_{j=1}^W w'_i \frac{\partial}{\partial x'_i} \kappa\left(\frac{x'_i - j\Delta}{\Delta}\right) v_{h_j}, \quad (12)$$

where $\tilde{v}_{x'_i}$ is the synthesized cotangent vector, (a) relies on integration-by-parts, $l'(x) = \frac{dl(x)}{dx}$ and

$$\kappa(x) = \int_{\mathbb{R}} l(y) k(x - y) dy = (l * k)(x). \quad (13)$$

In other words, the synthesized weak derivative of h_j is

$$\frac{\partial \tilde{h}_j}{\partial x'_i} = w'_i \frac{\partial}{\partial x'_i} \kappa\left(\frac{x'_i - j\Delta}{\Delta}\right). \quad (14)$$

Comparing Equation (14) with the formal derivative $\frac{\partial h_j}{\partial x'_i} = w'_i \frac{\partial}{\partial x'_i} k\left(\frac{x'_i - j\Delta}{\Delta}\right)$, we see that it's equal to a surrogate gradient of kernel $\kappa(\cdot)$. It's possible to demonstrate the unbiasedness of our method using the concept of weak derivatives, compared to other heuristic surrogates. In fact, it has finite-order approximation precision to long-range finite differences of arbitrary targets. Detailed proofs are provided in the appendix. For the multidimensional case in Equation (5), the result also holds when to replace k_d with κ_d for each dimension. Implementation is provided in the following section.

3.3 ALGORITHM IMPLEMENTATION

To simplify the implementation of FBP despite the theoretical density, we observe that our method only modifies the backward pass gradient accumulation. To demonstrate how different dimensions interact, a 2D example Algorithm 1 illustrates that the discontinuous kernel derivative is substituted with the synthesized weak derivative $\kappa'(\cdot)$, while the forward pass remains unchanged.

Input: Locations $\mathbf{x}'_i = (x'_i, y'_i)$, weights w'_i , Grid params ($W \times H$, spacing Δ).
Input: Kernels: Binning k , Reconstruction l . **Optional:** Tangents $\dot{\mathbf{x}}'_i = (\dot{x}'_i, \dot{y}'_i)$, Adjoints \bar{H} .
Output: Frame $H \in \mathbb{R}^{W \times H}$. **Optional:** Tangent Frame \dot{H} , Gradients $\nabla_{\mathbf{x}'} \mathcal{L}$.

```

 $\kappa(u) \leftarrow (l * k)(u); \quad \kappa'(u) \leftarrow \frac{d}{du} \kappa(u); \quad // \text{Synthesize derivative kernel}$ 
 $H \leftarrow \text{Zeros}(W, H); \text{for } i \leftarrow 1 \text{ to } N \text{ do } // 1. \text{ Primal Pass: Standard Binning}$ 
  foreach bin index  $(u, v)$  in support of  $k$  around  $(x'_i, y'_i)$  do
     $d_x \leftarrow (x'_i - u\Delta)/\Delta; \quad d_y \leftarrow (y'_i - v\Delta)/\Delta \quad // \text{Norm. distances}$ 
     $H[u, v] \leftarrow H[u, v] + w'_i \cdot k(d_x) \cdot k(d_y);$ 
  end
end
if Tangents  $\dot{\mathbf{x}}'$  are provided then // 2. Forward Mode: Tangent Propagation
   $\dot{H} \leftarrow \text{Zeros}(W, H); \text{for } i \leftarrow 1 \text{ to } N \text{ do}$ 
    foreach bin index  $(u, v)$  in support of  $\kappa$  around  $(x'_i, y'_i)$  do
       $d_x \leftarrow (x'_i - u\Delta)/\Delta; \quad d_y \leftarrow (y'_i - v\Delta)/\Delta; \quad val_x \leftarrow \frac{1}{\Delta} \kappa'(d_x) \cdot \kappa(d_y) \cdot \dot{x}'_i;$ 
       $val_y \leftarrow \kappa(d_x) \cdot \frac{1}{\Delta} \kappa'(d_y) \cdot \dot{y}'_i; \quad \dot{H}[u, v] \leftarrow \dot{H}[u, v] + w'_i \cdot (val_x + val_y);$ 
    end
  end
end
if Adjoints  $\bar{H}$  are provided then // 3. Backward Mode: Adjoint Propagation
   $\nabla_{\mathbf{x}'} \mathcal{L} \leftarrow \text{Zeros}(N, 2); \text{for } i \leftarrow 1 \text{ to } N \text{ do}$ 
     $g_x \leftarrow 0; \quad g_y \leftarrow 0; \text{foreach bin index } (u, v) \text{ in support of } \kappa \text{ around } (x'_i, y'_i) \text{ do}$ 
       $d_x \leftarrow (x'_i - u\Delta)/\Delta; \quad d_y \leftarrow (y'_i - v\Delta)/\Delta;$ 
       $g_x \leftarrow g_x + \bar{H}[u, v] \cdot w'_i \cdot \frac{1}{\Delta} \kappa'(d_x) \cdot \kappa(d_y);$ 
       $g_y \leftarrow g_y + \bar{H}[u, v] \cdot w'_i \cdot \kappa(d_x) \cdot \frac{1}{\Delta} \kappa'(d_y);$ 
    end
     $(\nabla_{\mathbf{x}'} \mathcal{L})_i \leftarrow (g_x, g_y);$ 
  end
end
return  $H, \dot{H}, \nabla_{\mathbf{x}'} \mathcal{L}$ 
```

Algorithm 1: 2D Functional Binning: Primal, Forward Mode (JVP), and Backward Mode (VJP)

3.4 BIAS ANALYSIS

Before applying the method to complex tasks, we explicitly validate its ability to approximate long-range finite differences. Following the methodology of (Gallego et al., 2019), we proceed with the following steps for an event packet $\{e_k = (x_k, y_k, t_k, p_k)\}_{k=1}^{N_e}$.

1. Events are warped to the mean time using rotational models:

$$T_{rot} : e_k \mapsto (t_{ref} - t)\omega \times \mathbf{x}_k + \mathbf{x}_k, \quad \mathbf{x}_k = (x_k, y_k, 1) \mapsto \mathbf{x}'_k. \quad (15)$$

2. An Image of Warped Events (IWE) of resolution 200×150 is constructed using non-differentiable (*rect*), differentiable (*linear*), and biased (*gauss*) binning kernels:

$$k_{rect}(x) = \mathbb{1}_{|x| < \frac{1}{2}}, \quad k_{linear}(x) = (1 - |x|)\mathbb{1}_{|x| < 1}, \quad k_{gauss}(x) = \frac{1}{\sqrt{2\pi}} e^{-x^2/2} \mathbb{1}_{|x| < \frac{3}{2}}. \quad (16)$$

3. Synthesized gradients are computed with $l(x) = \max(1 - |x|, 0)$ with respect to Variance (Var) (Gallego et al., 2018) and Log-Likelihood (LL) (Gu et al., 2021) scores:

$$\text{Var} = \frac{1}{N_p} \sum_{i,j} (h_{i,j} - \mu_H)^2, \quad \text{LL} = \sum_{i,j} \log(\text{NB}(h_{i,j} | r, p)), \quad (17)$$

where μ_H is the frame mean, and $(r, p) = (0.3, 0.8)$. Theoretical results show that this rectangular kernel has second-order accuracy in approximating the gradient of a score.

We analyze bias using 20,000 events from the *dynamic_rotation* sequence of the Event Camera Dataset (ECD) (Mueggler et al., 2017). A uniform grid of candidate angular velocities is sampled within $[-5, 5]^3$, yielding 1,331 score evaluations and 3,993 analytic gradients. Finite-difference bias is estimated by subtracting numerical gradients computed via central difference with a step size of 1.0. The results are shown in Figure 3.

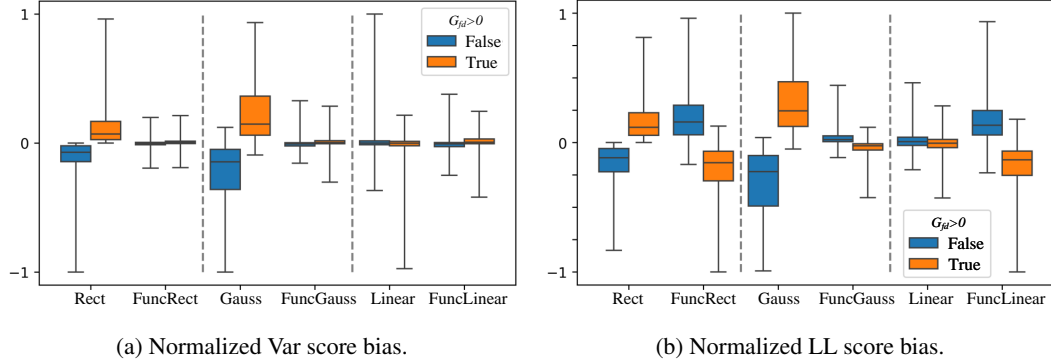


Figure 3: Bias analysis results. The analytical gradients are subtracted by numerical gradients to obtain the finite-difference bias, **colored by the sign of finite-difference gradients G_{fd}** .

As shown in Figure 3(a), the variance score exhibits strong bias with the *rect* and *gauss* kernels due to discontinuities, while the *linear* kernel remains unbiased. Our gradient estimation substantially reduces bias across all kernels, even improving the *linear* kernel by better approximating long-range finite differences.

For the log-likelihood score (Figure 3(b)), results are mixed: *rect* kernel bias is reduced at the cost of higher variance, while the *linear* kernel bias increases. Consistent with our theoretical analysis, this reflects the limited second-order accuracy of the triangular reconstruction $l(x)$ in approximating the nonlinear LL score. This suggests the exact gradient estimation method should be application-dependent, which our framework supports via adaptable cotangent reconstruction constraints.

4 EXPERIMENTS

This section further validates the proposed method on event-based motion estimation tasks, specifically angular and linear velocity estimation, where the computed gradients guide the optimization. Besides the rotational motion model defined in Equation (15), we introduce a linear motion model:

$$T_{trans} : e_k \mapsto (t_{ref} - t)\mathbf{v} + \mathbf{x}_k, \quad \mathbf{x}_k = (x_k, y_k, 1) \mapsto \mathbf{x}'_k. \quad (18)$$

We evaluate all model–kernel–score combinations on eight sequences from the Event Camera Dataset (ECD), namely *boxes*, *dynamic*, *poster*, and *shapes* (both rotation and translation). The sequences are partitioned into non-overlapping packets of $N_e = 20,000$ events to estimate motion parameters. Accuracy is quantified using Root Mean Square (RMS) error in %/s for rotation and m/s for translation. Images of Warped Events (IWEs) are constructed from projected coordinates with a resolution of 200×150 and a binning step of $\Delta = 0.01$. Experiments were conducted on a laptop equipped with an NVIDIA RTX 4090 GPU using the JAX framework (Bradbury et al., 2018). We employed distinct optimizers tailored to the kernel properties: L-BFGS-B (Liu & Nocedal, 1989) for the *rect* and *linear* kernels, and trust-ncg (Steihaug, 1983) for the *gauss* kernel.

4.1 OPTIMIZATION RESULTS

The mean performance across all sequences is presented in Figure 4. It is evident that our method improves both accuracy and convergence speed for angular velocity estimation, achieving a 10.3% reduction in RMS error and a $1.66 \times$ acceleration in convergence. In the case of linear velocity,

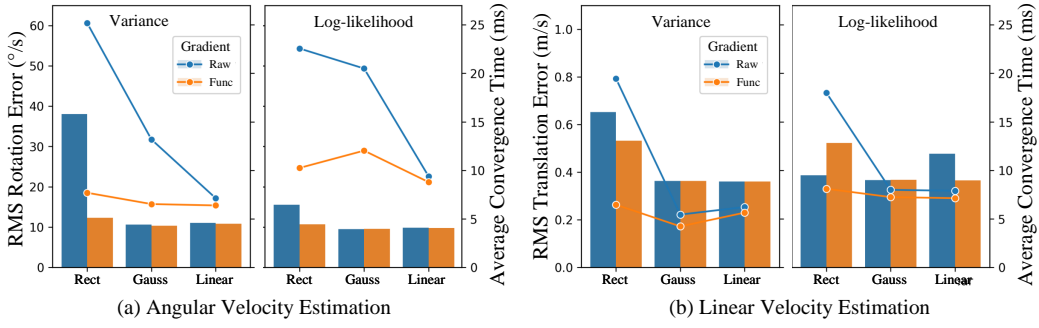


Figure 4: Optimization results for motion estimation, with combined bar charts showing RMS estimation accuracy and line charts showing the mean convergence time for every $N_e = 20000$ events.

singularities of this task (Guo & Gallego, 2024) lead to a marginal 3.9% increase in RMS error, yet the method maintains a $1.48\times$ faster convergence rate. Overall, the proposed method yields a 3.2% improvement in RMS error alongside a $1.57\times$ speedup. Since our approach modifies only the gradients without altering the solution space, these performance gains indicate that our synthesized gradients provide more effective update directions. Although the gradient computation incurs higher theoretical complexity (Equation (13)), the empirical results demonstrate that this cost is outweighed by the benefits in optimization efficiency. For complete results, please refer to the appendix.

4.2 ABLATION STUDIES AND BASELINE COMPARISONS

This subsection investigates the efficacy of Functional Backpropagation (FBP) using the linear reconstruction kernel. To isolate the effects of the reconstruction method, we focus on the rotational case utilizing the k_{rect} binning kernel and the Var and LL score function.

Sensitivity to Reconstruction Kernels. For the reconstruction kernel $l(x)$, we additionally evaluate the Cubic kernel (assuming a C^2 smooth cotangent function) and the Lanczos kernel (assuming a band-limited cotangent function), defined as:

$$l_{Cubic}(x) = \begin{cases} 1.5|x|^3 - 2.5|x|^2 + 1 & |x| < 1 \\ 2.5|x|^2 - 0.5|x|^3 - 4|x| + 2 & 1 < |x| \leq 2 \\ 0 & \text{otherwise} \end{cases}, \quad (19)$$

$$l_{Lanczos}(x) = \frac{2 \sin(\pi x) \sin(\frac{\pi}{2}x)}{\pi^2 x^2} \mathbb{1}_{|x| \leq 2}.$$

Table 1: **Ablation study on reconstruction kernels.** Different cotangent reconstruction kernels are compared in angular velocity estimation in Accuracy/Time (°/s and ms). **Bold:** best value.

Kernel	boxes_rotation		dynamic_rotation		poster_rotation		shapes_rotation	
	Var	LL	Var	LL	Var	LL	Var	LL
Bicubic	12.47/7.37	10.17/9.17	6.70/8.56	5.88/10.78	14.39/7.61	12.48/9.54	16.47/11.31	13.82 /18.07
Lanczos	12.46/8.84	10.10 /10.12	6.72/10.36	5.86 /12.37	14.15 /9.01	12.45/10.66	17.93/14.83	14.25/21.12
Linear	12.44/6.50	10.14/8.07	6.67/7.44	5.88/9.57	14.26/6.55	12.42/8.17	15.89/10.26	14.26/ 15.18

As shown in Table 1, the Linear kernel achieves the optimal trade-off between accuracy and efficiency. While higher-order kernels offer greater smoothness, they increase computational runtime with diminishing returns in estimation accuracy. Consequently, we utilize the Linear reconstruction kernel for the remainder of our experiments.

Comparison vs. Heuristic Surrogate Gradients (SG). We compare FBP against standard Surrogate Gradients commonly used in Spiking Neural Networks: the Straight-Through-Estimator (STE) (Yin et al., 2019) and the Sigmoid Surrogate (Neftci et al., 2019), defined as:

$$\kappa'_{STE} = -\text{sgn}(x) \mathbb{1}_{|x| < 1}, \quad \kappa'_{sigmoid} = \sigma'(10(x + \frac{1}{2})) - \sigma'(10(x - \frac{1}{2})), \quad \sigma(x) = \frac{1}{1 + \exp(-x)}. \quad (20)$$

Table 2: **Comparisons with heuristic surrogate gradients.** Different gradient surrogates are compared in angular velocity estimation in Accuracy/Time (°/s and ms). **Best**: Best value.

Surrogate	boxes_rotation		dynamic_rotation		poster_rotation		shapes_rotation	
	Var	LL	Var	LL	Var	LL	Var	LL
STE	36.29/7.18	14.32/8.88	10.92/8.45	9.00/10.36	29.00/7.38	16.22/8.91	96.89/ 13.07	55.83/ 17.35
Sigmoid	13.94/7.55	10.17/8.49	7.12/8.74	5.88/9.84	15.60/7.70	12.51/8.68	18.76/11.41	14.23/15.44
FBP (Ours)	12.44/6.50	10.14/8.07	6.67/7.44	5.88/9.57	14.26/6.55	12.42/8.17	15.89/10.26	14.26/ 15.18

From Table 2, FBP achieves a significantly lower error floor and reduced convergence time compared to heuristic SGs. This confirms that deriving the gradient via integration by parts captures the underlying binning geometry more effectively than imposing arbitrary smooth shapes.

4.3 COMPUTATIONAL COMPLEXITY

To supplement the optimization analysis in Section 4.1, we verify the computational cost of the proposed method by comparing the execution time of a single call to the original binning function versus the gradient computation function. As Jacobian-vector products (JVPs) inherit the structure of the forward pass without requiring intermediate storage, we present the computation time for a single JVP call in float32 on both CPU and GPU in Table 3, where our method for different binning kernels is prefixed with Func. The data indicates that the computation time approximately doubles compared to the standard deduced JVP. However, when combined with the optimization results in Section 4.1, the overall efficiency and effectiveness of the method are confirmed.

Table 3: Computation time in microseconds. Our modified gradient computation is shown in **bold**.

Platforms	CPU (R9-7945HX)			GPU (4090-laptop)		
	20000	50000	100000	20000	50000	100000
Rect	37.1	69.9	110	31.1	29.6	29.7
FuncRect JVP	635	893	1440	42.3	62.4	78.8
Gauss	536	820	1380	44.9	61.7	75.6
Gauss JVP	638	946	1600	40.6	62.3	77.7
FuncGauss JVP	1090	2130	5890	83.5	114	158
Overhead	1.71 ×	2.25 ×	3.68 ×	2.06 ×	1.83 ×	2.03 ×
Linear	473	551	774	26.8	37.1	55.6
Linear JVP	440	543	772	28.1	37.3	51.5
FuncLinear JVP	736	1190	2120	66.8	83.1	117
Overhead	1.67 ×	2.19 ×	2.75 ×	2.38 ×	2.23 ×	2.27 ×

5 APPLICATIONS

To test the applicability of the proposed gradient computation method on modern learning pipelines, we conduct further experiments on the latest event-based optical flow estimation network MotionPriorCMax (Hamann et al., 2024) and SLAM algorithm CMax-SLAM (Guo & Gallego, 2024).

5.1 MOTIONPRIORCMAX

MotionPriorCMax (MPC) is the SOTA self-supervised optical flow estimation network that uses the linear binning kernel k_2 to construct a contrast loss for learning, which is trained against the latest DSEC (Gehrig et al., 2021a) dataset. We changed the binning kernel to k_{rect} using the modified gradient computation method and retrained the model on eight RTX A6000 GPUs. Reported metrics are End Point Error (EPE), Angular Error (AE), and percentage of outliers with $EPE > 3px$ (3PE).

Results. We present the average DSEC benchmark performance in Figure 5 where our method improves the EPE error by 9.4%, confirming that the new gradient computation method helps to find the optimal parameters even for a complex neural network. A visualization presented in the right

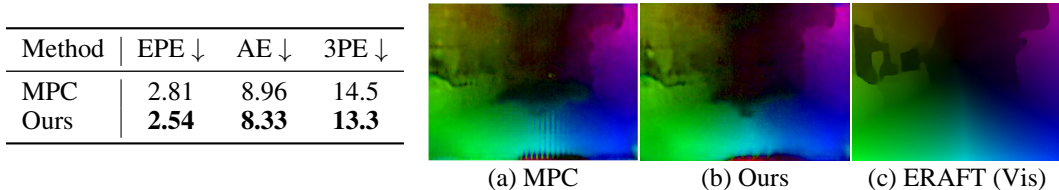


Figure 5: **Left:** all sequence average performance on DSEC. **Right:** Predicted optical flow (ERAFT only for qualitative visualization). Our method exhibits more robustness with fewer artifacts.

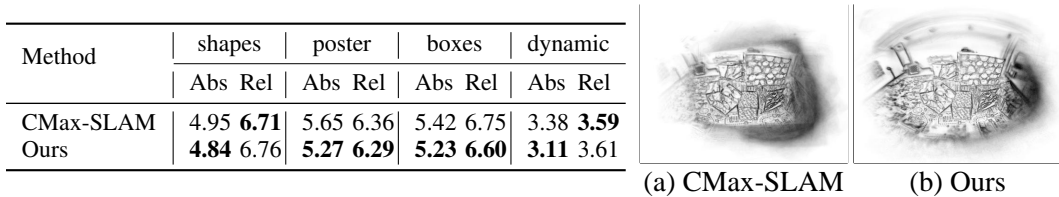


Figure 6: **Left:** CMax-SLAM results on real-world sequences from ECD. We report Absolute (Abs) and Relative (Rel) trajectory errors (best results in **bold**). **Right:** Mapping result on the full sequence, showing that CMax-SLAM fails on long sequences while our method preserves correctness.

of Figure 5, where optical flow output by ERAFT (Gehrig et al., 2021b) is regarded as ground truth since it is not available on test sequences. It’s observed that the network learns more robust features with a sharper IWE, which is only trainable with our method. For a complete result on all 7 test sequences, please refer to the appendix.

5.2 CMAX-SLAM

CMax-SLAM (Guo & Gallego, 2024) is the SOTA rotation-only SLAM algorithm that uses the Contrast Maximization framework (Gallego et al., 2018) on both the frontend and backend, where a panoramic IWE is constructed as the map. We changed the binning kernel from k_{linear} to k_{rect} and report the RMS absolute trajectory error (Abs) in [$^\circ$] and the RMS relative error (Rel) in [$^\circ/s$] for the first 30s of data of the sequences in ECD (Mueggler et al., 2017) for a fair comparison.

Results. The overall ECD benchmark results are shown in Figure 6, where our method mainly improves the Abs RMS error by 5.1% with comparable Rel RMS error. On the right side of Figure 6, we show the reconstruction results of the two methods: the baseline fails on long sequences due to accumulated errors, while our method preserves correctness and yields more robust reconstructions, showing that sharp IWE helps reduce the mapping ambiguity.

6 CONCLUSION

In this work, we addressed the long-standing challenge of biased gradient estimation in event binning for event-based vision. By lifting binning functions to the functional space and leveraging weak derivatives through integration by parts, we derived an exact formula for synthesizing unbiased gradients. This framework, termed **Functional Backpropagation**, reconstructs cotangent functions during backpropagation and guarantees unbiasedness without altering the forward outputs. Our theoretical analysis established the correctness and unbiasedness of the synthesized gradients, while extensive experiments on motion estimation, optical flow, and SLAM demonstrated consistent improvements in both accuracy and convergence speed. Looking forward, our framework opens up opportunities to extend unbiased gradient estimation to a wider class of discontinuous operators in neuromorphic computing and to generalizations to nonuniform binning grids and nonlinear reconstruction methods.

ACKNOWLEDGEMENTS

This work is supported by the National Natural Science Foundation of China (NSFC) under Grants 62225207, 62436008, 62306295, and 62576328. The AI-driven experiments, simulations and model training were performed on the robotic AI-Scientist platform of Chinese Academy of Sciences.

REFERENCES

James Bradbury, Roy Frostig, Peter Hawkins, Matthew James Johnson, Chris Leary, Dougal Maclaurin, George Necula, Adam Paszke, Jake VanderPlas, Skye Wanderman-Milne, and Qiao Zhang. JAX: composable transformations of Python+NumPy programs, 2018. URL <http://github.com/jax-ml/jax>.

Jason K Eshraghian, Max Ward, Emre O Neftci, Xinxin Wang, Gregor Lenz, Girish Dwivedi, Mohammed Bennamoun, Doo Seok Jeong, and Wei D Lu. Training spiking neural networks using lessons from deep learning. *Proceedings of the IEEE*, 111(9):1016–1054, 2023.

Béla A Frigyik, Santosh Srivastava, and Maya R Gupta. An introduction to functional derivatives. *Dept. Electr. Eng., Univ. Washington, Seattle, WA, Tech. Rep*, 1, 2008.

Guillermo Gallego, Henri Rebucq, and Davide Scaramuzza. A unifying contrast maximization framework for event cameras, with applications to motion, depth, and optical flow estimation. In *Proceedings of the IEEE conference on computer vision and pattern recognition*, pp. 3867–3876, 2018.

Guillermo Gallego, Mathias Gehrig, and Davide Scaramuzza. Focus is all you need: Loss functions for event-based vision. In *Proceedings of the IEEE/CVF Conference on Computer Vision and Pattern Recognition*, pp. 12280–12289, 2019.

Guillermo Gallego, Tobi Delbrück, Garrick Orchard, Chiara Bartolozzi, Brian Taba, Andrea Censi, Stefan Leutenegger, Andrew J Davison, Jörg Conradt, Kostas Daniilidis, et al. Event-based vision: A survey. *IEEE transactions on pattern analysis and machine intelligence*, 44(1):154–180, 2020.

Mathias Gehrig, Willem Aarents, Daniel Gehrig, and Davide Scaramuzza. Dsec: A stereo event camera dataset for driving scenarios. *IEEE Robotics and Automation Letters*, 6(3):4947–4954, 2021a.

Mathias Gehrig, Mario Millhäuser, Daniel Gehrig, and Davide Scaramuzza. E-raft: Dense optical flow from event cameras. In *2021 International Conference on 3D Vision (3DV)*, pp. 197–206. IEEE, 2021b.

Suman Ghosh and Guillermo Gallego. Event-based stereo depth estimation: A survey. *IEEE Transactions on Pattern Analysis and Machine Intelligence*, 2025.

Cheng Gu, Erik Learned-Miller, Daniel Sheldon, Guillermo Gallego, and Pia Bideau. The spatio-temporal poisson point process: A simple model for the alignment of event camera data. In *Proceedings of the IEEE/CVF International Conference on Computer Vision*, pp. 13495–13504, 2021.

Shuang Guo and Guillermo Gallego. Cmax-slam: Event-based rotational-motion bundle adjustment and slam system using contrast maximization. *IEEE Transactions on Robotics*, 40:2442–2461, 2024.

Friedhelm Hamann, Ziyun Wang, Ioannis Asmanis, Kenneth Chaney, Guillermo Gallego, and Kostas Daniilidis. Motion-prior contrast maximization for dense continuous-time motion estimation. In *European Conference on Computer Vision*, pp. 18–37. Springer, 2024.

Han Han, Wei Zhai, Yang Cao, Bin Li, and Zheng-jun Zha. Mate: Motion-augmented temporal consistency for event-based point tracking. In *Proceedings of the IEEE/CVF International Conference on Computer Vision (ICCV)*, pp. 8340–8349, October 2025.

Adam D Hines, Michael Milford, and Tobias Fischer. A compact neuromorphic system for ultra-energy-efficient, on-device robot localization. *Science Robotics*, 10(103):eads3968, 2025.

Dongsung Huh and Terrence J Sejnowski. Gradient descent for spiking neural networks. *Advances in neural information processing systems*, 31, 2018.

Kenneth Kuttler. Weak derivatives. In *Modern Analysis* (1997), pp. 355–370. CRC Press, 2017.

Xavier Lagorce, Garrick Orchard, Francesco Galluppi, Bertram E Shi, and Ryad B Benosman. Hots: a hierarchy of event-based time-surfaces for pattern recognition. *IEEE transactions on pattern analysis and machine intelligence*, 39(7):1346–1359, 2016.

Bohao Liao, Wei Zhai, Zengyu Wan, Zhixin Cheng, Wenfei Yang, Yang Cao, Tianzhu Zhang, and Zheng-Jun Zha. EF-3DGS: Event-aided free-trajectory 3d gaussian splatting. In *The Thirty-ninth Annual Conference on Neural Information Processing Systems*, 2025. URL <https://openreview.net/forum?id=shFhW4zqd6>.

Dong C Liu and Jorge Nocedal. On the limited memory bfgs method for large scale optimization. *Mathematical programming*, 45(1):503–528, 1989.

Xinglong Luo, Ao Luo, Zhengning Wang, Chunyu Lin, Bing Zeng, and Shuaicheng Liu. Efficient meshflow and optical flow estimation from event cameras. In *Proceedings of the IEEE/CVF Conference on Computer Vision and Pattern Recognition*, pp. 19198–19207, 2024.

Xinglong Luo, Ao Luo, Kunming Luo, Zhengning Wang, Ping Tan, Bing Zeng, and Shuaicheng Liu. Learning efficient meshflow and optical flow from event cameras. *IEEE Transactions on Pattern Analysis and Machine Intelligence*, 2025.

Ana I Maqueda, Antonio Loquercio, Guillermo Gallego, Narciso García, and Davide Scaramuzza. Event-based vision meets deep learning on steering prediction for self-driving cars. In *Proceedings of the IEEE conference on computer vision and pattern recognition*, pp. 5419–5427, 2018.

Elias Mueggler, Henri Rebecq, Guillermo Gallego, Tobi Delbruck, and Davide Scaramuzza. The event-camera dataset and simulator: Event-based data for pose estimation, visual odometry, and slam. *The International journal of robotics research*, 36(2):142–149, 2017.

Emre O Neftci, Hesham Mostafa, and Friedemann Zenke. Surrogate gradient learning in spiking neural networks: Bringing the power of gradient-based optimization to spiking neural networks. *IEEE Signal Processing Magazine*, 36(6):51–63, 2019.

Liyuan Pan, Cedric Scheerlinck, Xin Yu, Richard Hartley, Miaomiao Liu, and Yuchao Dai. Bringing a blurry frame alive at high frame-rate with an event camera. In *Proceedings of the IEEE/CVF conference on computer vision and pattern recognition*, pp. 6820–6829, 2019.

Adam Paszke, Sam Gross, Soumith Chintala, Gregory Chanan, Edward Yang, Zachary DeVito, Zeming Lin, Alban Desmaison, Luca Antiga, and Adam Lerer. Pytorch: An imperative style, high-performance deep learning library. In *Advances in Neural Information Processing Systems*, volume 32, 2019.

Henri Rebecq, René Ranftl, Vladlen Koltun, and Davide Scaramuzza. High speed and high dynamic range video with an event camera. *IEEE transactions on pattern analysis and machine intelligence*, 43(6):1964–1980, 2019.

Zekun Shi, Zheyuan Hu, Min Lin, and Kenji Kawaguchi. Stochastic taylor derivative estimator: Efficient amortization for arbitrary differential operators. *Advances in Neural Information Processing Systems*, 37:122316–122353, 2024.

Shintaro Shiba, Friedhelm Hamann, Yoshimitsu Aoki, and Guillermo Gallego. Event-based background-oriented schlieren. *IEEE transactions on pattern analysis and machine intelligence*, 46(4):2011–2026, 2023.

Shintaro Shiba, Yannick Klose, Yoshimitsu Aoki, and Guillermo Gallego. Secrets of event-based optical flow, depth, and ego-motion by contrast maximization. *IEEE Trans. Pattern Anal. Mach. Intell. (T-PAMI)*, pp. 1–18, 2024. doi: 10.1109/TPAMI.2024.3396116.

Trond Steihaug. The conjugate gradient method and trust regions in large scale optimization. *SIAM Journal on Numerical Analysis*, 20(3):626–637, 1983.

Minggui Teng, Chu Zhou, Hanyue Lou, and Boxin Shi. Nest: Neural event stack for event-based image enhancement. In *European Conference on Computer Vision*, pp. 660–676. Springer, 2022.

Stepan Tulyakov, Daniel Gehrig, Stamatios Georgoulis, Julius Erbach, Mathias Gehrig, Yuanyou Li, and Davide Scaramuzza. Time lens: Event-based video frame interpolation. In *Proceedings of the IEEE/CVF conference on computer vision and pattern recognition*, pp. 16155–16164, 2021.

Antoni Rosinol Vidal, Henri Rebucq, Timo Horstschaefer, and Davide Scaramuzza. Ultimate slam? combining events, images, and imu for robust visual slam in hdr and high-speed scenarios. *IEEE Robotics and Automation Letters*, 3(2):994–1001, 2018.

Zengyu Wan, Ganchao Tan, Yang Wang, Wei Zhai, Yang Cao, and Zheng-Jun Zha. Event-based optical flow via transforming into motion-dependent view. *IEEE Transactions on Image Processing*, 33:5327–5339, 2024.

Zengyu Wan, Wei Zhai, Yang Cao, and Zhengjun Zha. Emotive: Event-guided trajectory modeling for 3d motion estimation. In *Proceedings of the IEEE/CVF International Conference on Computer Vision (ICCV)*, pp. 9342–9351, October 2025.

Yuliang Wu, Ganchao Tan, Jinze Chen, Wei Zhai, Yang Cao, and Zheng-Jun Zha. Event-based asynchronous hdr imaging by temporal incident light modulation. *Optics Express*, 32(11):18527–18538, 2024.

Senyan Xu, Zhijing Sun, Mingchen Zhong, Chengzhi Cao, Yidi Liu, Xueyang Fu, and Yan Chen. Motion-adaptive transformer for event-based image deblurring. In *Proceedings of the AAAI Conference on Artificial Intelligence*, volume 39, pp. 8942–8950, 2025.

Penghang Yin, Jiancheng Lyu, Shuai Zhang, Stanley J. Osher, Yingyong Qi, and Jack Xin. Understanding straight-through estimator in training activation quantized neural nets. In *International Conference on Learning Representations*, 2019. URL <https://openreview.net/forum?id=Skh4jRcKQ>.

Yi Zhou, Guillermo Gallego, and Shaojie Shen. Event-based stereo visual odometry. *IEEE Transactions on Robotics*, 37(5):1433–1450, 2021.

Alex Zhu, Liangzhe Yuan, Kenneth Chaney, and Kostas Daniilidis. Ev-flownet: Self-supervised optical flow estimation for event-based cameras. In *Proceedings of Robotics: Science and Systems*, Pittsburgh, Pennsylvania, June 2018. doi: 10.15607/RSS.2018.XIV.062.

A APPENDIX

A.1 USE OF LLMs

This paper uses ChatGPT only for text polishing, correcting mathematical symbols, and searching relevant work. The surrogate gradient (SG) method is one that was new knowledge to the authors and provides useful insights into the presentation of this paper.

A.2 FUNCTIONAL AUTOMATIC DIFFERENTIATION

This section supplements the discussion in Section 3.1 to cover general automatic differentiation, and to make the text self-contained with the necessary mathematical results proved.

To simplify the expression of functional automatic differentiation, we introduce the following conventions:

- **Vertical bar notation.** For an operator f , we write

$$f(u|y) := [f(u)](y),$$

meaning that f takes a function $u \in \mathcal{H}(X)$ as input, produces a function in $\mathcal{H}(Y)$, and then we evaluate this function at $y \in Y$. This notation is non-standard, but convenient for distinguishing between function mapping and function evaluation. Given no risk of ambiguity, we may write $f(y) := f(u|y)$ for brevity.

- **Variational symbol δ .** We use δ in analogy to Leibniz’s differential d , but acting on functions instead of scalar values. The quotient

$$\frac{\delta f(y)}{\delta g(x)}$$

denotes the *operator derivative* of $f(y)$ with respect to $g(x)$.

A.2.1 THE CHAIN RULE OF FUNCTIONALS

Fundamental to automatic differentiation is the decomposition of differentials provided by the chain rule of partial derivatives of composite functions. However, since functionals are functions that consume an entire function to give a value, the input dimension is infinite, so the derivatives cannot be expressed by finite-dimensional Jacobian matrices. To extend the chain rule to functionals, remember that derivatives are unique local linear approximations to the function. This leads to the definition of the Fréchet derivative:

Definition 2 (Fréchet). *Let V and W be normed vector spaces, and $U \subseteq V$ be an open subset of V . A function $f : U \rightarrow W$ is called Fréchet differentiable at $x \in U$ if there exists a bounded linear operator $A : V \rightarrow W$ such that*

$$\lim_{\|h\|_V \rightarrow 0} \frac{\|f(x + h) - f(x) - Ah\|_W}{\|h\|_V} = 0. \quad (21)$$

If there exists such an operator A , it is unique, so we write $Df[x] = A$ and call it the Fréchet derivative of f at x . A function f is Fréchet differentiable if $\forall x \in U$, $Df[x]$ exists.

For the Fréchet derivative, the well-known Fermat’s theorem also applies to identify critical points of a given functional by solving an equation involving the derivative. This result makes it possible to treat the Fréchet derivative like an ordinary derivative when solving an optimization problem.

Theorem 2 (Fermat). *Let V be a normed vector space and $f : V \rightarrow \mathbb{R}$ is a functional that is Fréchet differentiable on V . Then if x_0 is a point where f has a local extremum, $Df[x_0] = \mathbf{0}$ (the zero functional).*

Proof. Without loss of generality, let x_0 be the local maxima. Then there exists $\delta > 0$ such that when $\|h\|_V < \delta$,

$$f(x_0 + h) \leq f(x_0). \quad (22)$$

According to Definition 2, we have

$$f(x_0 + h) - f(x_0) - Df[x_0](h) = o(\|h\|_V). \quad (23)$$

For all $v \in V$, we can find a t that satisfy $\|tv\|_V < \delta$, substitute h for tv :

$$f(x_0 + tv) - f(x_0) = t \cdot Df[x_0](v) + o(|t|) \leq 0. \quad (24)$$

Taking $t \rightarrow 0^+$, gives $Df[x_0](v) \leq 0$, likewise with $t \rightarrow 0^-$, we have $Df[x_0](v) \geq 0$. Thus $Df[x_0](v) = 0, \forall v \in V$ and hence $Df[x_0] = 0$. \square

The chain rule has an analogous form as ordinary derivative, but expressed as composition of linear operators.

Theorem 3 (The Chain Rule). *Let U, V and W be normed vector spaces and $U \xrightarrow{f} V \xrightarrow{g} W$. If f is Fréchet differentiable at $u \in U$ and g is Fréchet differentiable at $f(u) \in V$, then the composite function $h = g \circ f$ is Fréchet differentiable at u with the chain rule*

$$Dh[u] = Dg[f(u)] \circ Df[u]. \quad (25)$$

Proof. From Definition 2, we have for a small perturbation δu such that h is differentiable at $u + \delta u$,

$$h(u + \delta u) = g(f(u + \delta u)), \quad (26)$$

$$= g(f(u) + Df[u](\delta u) + r_f(\delta u)), \quad (27)$$

$$= h(u) + Dg[f(u)](Df[u](\delta u)) + Dg[f(u)](r_f(\delta u)) + r_g(Df[u](\delta u) + r_f(\delta u)), \quad (28)$$

such that $\lim_{\varepsilon \rightarrow 0} \frac{\|r_f(\varepsilon)\|_V}{\|\varepsilon\|_U} = 0$, and $\lim_{\eta \rightarrow 0} \frac{\|r_g(\eta)\|_W}{\|\eta\|_V} = 0$. Since $Df[u]$ and $Dg[f(u)]$ are bounded, there exist constants C_1 and C_2 such that $\|Df[u](\varepsilon)\|_V \leq C_1 \|\varepsilon\|_U$ and $\|Dg[f(u)](\eta)\|_W \leq C_2 \|\eta\|_V$. So for the remainder, we have

$$\frac{\|Dg[f(u)](r_f(\delta u))\|_W}{\|\delta u\|_U} \leq C_2 \frac{\|r_f(\delta u)\|_V}{\|\delta u\|_U} \rightarrow 0 \quad (29)$$

and

$$\frac{\|r_g(Df[u](\delta u) + r_f(\delta u))\|_W}{\|\delta u\|_U} = \frac{\|r_g(Df[u](\delta u) + r_f(\delta u))\|_W}{\|Df[u](\delta u) + r_f(\delta u)\|_V} \frac{\|Df[u](\delta u) + r_f(\delta u)\|_V}{\|\delta u\|_U}, \quad (30)$$

$$\leq \frac{\|r_g(Df[u](\delta u) + r_f(\delta u))\|_W}{\|Df[u](\delta u) + r_f(\delta u)\|_V} (C_1 + \frac{\|r_f(\delta u)\|_V}{\|\delta u\|_U}) \rightarrow 0. \quad (31)$$

So $h(u + \delta u) = h(u) + (Dg[f(u)] \circ Df[u])(\delta u) + o(\|\delta u\|_U)$. \square

In automatic differentiation, closed-form expressions are required rather than abstract operators. To derive this, we add the additional constraint that all vector spaces are Hilbert spaces, so that we can apply the **Riesz Representation Theorem**. To simplify the expression, we introduce a new notation analogous to Leibniz's notation for operators.

Theorem 4 (Riesz). *Denote $H(X) = L^2(X) \cap C(X)$ as the space of continuous and square-integrable functions on X . Let $H(X) \xrightarrow{f} H(Y) \xrightarrow{g} H(Z)$, f is Fréchet differentiable in $H(X)$ and g is Fréchet differentiable in $H(Y)$. Denote point evaluation functionals on $H(Y)$ and $H(Z)$ as $L_y : v \mapsto v(y), \forall v \in H(Y)$ and $L_z : w \mapsto w(z), \forall w \in H(Z)$ respectively and the Riesz representation of $D(L_y \circ f)[u]$ as $\frac{\delta f(u|y)}{\delta I(u|x)}$, where I represents the identity mapping, then the Riesz representation of composite functional $D(L_z \circ g \circ f)[u]$ is:*

$$\frac{\delta g(f(u)|z)}{\delta I(u|x)} = \int_Y \frac{\delta g(f(u)|z)}{\delta f(u|y)} \frac{\delta f(u|y)}{\delta I(u|x)} dy. \quad (32)$$

Proof. From the definition, L_* is a linear operator so $DL_*[\cdot] = L_*$. $D(L_z \circ g \circ f)[u] = L_z \circ Dg[f(u)] \circ Df[u]$ from the chain rule, then $\forall v \in H(X)$, we have

$$L_z \circ Dg[f(u)] \circ Df[u](v) = \int_Y \frac{\delta g(f(u)|z)}{\delta f(u|y)} (Df[u](v))(y) dy, \quad (33)$$

$$= \int_Y \frac{\delta g(f(u)|z)}{\delta f(u|y)} (L_y \circ Df[u])(v) dy, \quad (34)$$

$$= \int_Y \frac{\delta g(f(u)|z)}{\delta f(u|y)} dy \int_X \frac{\delta f(u|y)}{\delta I(u|x)} v(x) dx, \quad (35)$$

$$= \int_{X \times Y} \frac{\delta g(f(u)|z)}{\delta f(u|y)} \frac{\delta f(u|y)}{\delta I(u|x)} v(x) dx dy. \quad (36)$$

Since $v \in H(X)$ is arbitrary, the theorem is proved. \square

A.2.2 INTERPRETATION OF AUTOMATIC DIFFERENTIATION OF FUNCTIONALS

In ordinary AD, the task is to compute Jacobian-Vector products (forward mode) or Vector-Jacobian products (reverse mode) so that entries of the full Jacobian matrix can be computed by selecting the test vectors to be the standard basis $e^{(i)}$ in the tangent or cotangent spaces. In functional AD, the analogue is the integration of the product of the functional derivative representation and the tangent (cotangent) function.

Definition 3 (Functional Forward Mode AD). *Given a Fréchet differentiable function $f : H(X) \rightarrow H(Y)$ and tangent function at $u \in H(x)$ as $v \in T_u H(X)$, the functional forward mode AD program computes the tangent function at $f(u) \in H(Y)$ as $w \in T_{f(u)} H(Y)$.*

$$w(y) = \int_X \frac{\delta f(u|y)}{\delta I(u|x)} v(x) dx. \quad (37)$$

Definition 4 (Functional Reverse Mode AD). *Given a Fréchet differentiable function $f : H(X) \rightarrow H(Y)$ and cotangent function at $f(u) \in H(Y)$ as $w^* \in T_{f(u)}^* H(Y)$, the functional reverse mode AD program computes the cotangent function at $u \in H(X)$ as $v^* \in T_u^* H(X)$.*

$$v^*(x) = \int_Y \frac{\delta f(u|y)}{\delta I(u|x)} w^*(y) dy. \quad (38)$$

Now, with the formal definition of functional AD, it's possible to derive a recursive procedure to compute the Riesz representation of composite functionals:

Corollary 1. *Let $f_i : H(X_i) \rightarrow H(X_{i+1})$ be Fréchet differentiable in $H(X_i)$ and $F_n = f_{n-1} \circ f_{n-2} \circ \dots \circ f_1$. The functional forward mode AD states that the tangent function of F_n at $F_n(u)$ can be recursively computed as:*

$$w(x_{m+1}) = \int_{X_m} \frac{\delta f_m(F_m(u)|x_{m+1})}{\delta f_{m-1}(F_{m-1}(u)|x_m)} w(x_m) dx_m \quad (39)$$

and the functional reverse mode AD states that the cotangent function of F_n at u can be recursively computed as:

$$v^*(x_{m-1}) = \int_{X_m} \frac{\delta f_{m-1}(F_{m-1}(u)|x_m)}{\delta f_{m-2}(F_{m-2}(u)|x_{m-1})} v^*(x_m) dx_m \quad (40)$$

where we define $f_{-1} = f_0 = I$ as the identity map so $F_0 = F_1 = I$.

A.2.3 THE CONNECTION BETWEEN FUNCTIONS AND SAMPLED DIRAC COMBS

In Equation (11), we make an equation between the cotangent function and the sampled cotangent vector. This is understood in the distributional sense. In fact, we have:

Theorem 5. *For any smooth function $g(x) \in \mathcal{H}(\mathbb{R})$, if Equation (11) hold, we have:*

$$\lim_{\Delta \rightarrow 0} \int g(x) v_h(x) dx = \sum_{j=1}^W \int g(x) v_{h_j} \delta(x - j\Delta) dx. \quad (41)$$

Proof. Select simple functions $g(x) = \max(1 - |\frac{x-j\Delta}{\Delta}|, 0)$, the equation is proved by observing that the right-hand side constitutes the Riemann sum. As any smooth function can be approximated by summing such simple functions, the result is proved. \square

A.3 THE UNBIASEDNESS CONSTRAINT

The problem of ensuring unbiasedness is how to quantify the bias when the true gradients don't exist. To achieve that, we resort to line integrals so that the bias can be measured in the distributional sense. Let ϕ be an arbitrary smooth function that accepts a binned event frame $\mathbf{h} \in H_d$ to return a scalar $\phi(\mathbf{h})$, then by the fundamental theorem of calculus for line integrals, we have for every piecewise-smooth curve $\mathbf{h} : [a, b] \rightarrow H_d$:

$$\phi(\mathbf{h}(b)) - \phi(\mathbf{h}(a)) = \int_a^b \nabla \phi(\mathbf{h}(t)) \cdot \mathbf{h}'(t) dt, \quad (42)$$

where $\mathbf{h}'(t)$ should be understood in the weak sense. Assuming we want to find the optimal histogram parameters by inferring the extreme values of some smooth objective, then the derivative $\mathbf{h}'(t)$ is the only function that makes the above equation true. In this view, if the above equation is nearly true with $\tilde{\mathbf{h}}'(t)$, then we call it an unbiased gradient estimation.

For a simplified equation that can be used to check the unbiasedness, we pick each entry $h_j(t)$ inside the vector dot product and approximate $\nabla_j \phi(\mathbf{h}(t))$ with another arbitrary smooth function $\varphi_j(t)$, then the above argument translates to:

$$\int \varphi_j(t) h'_j(t) dt = - \int \varphi'_j(t) h_j(t) dt, \quad (43)$$

when $h_j \phi_n$ vanishes at the boundaries. Since there's no $\tilde{\mathbf{h}}'(t)$ other than $\mathbf{h}'(t)$ to ensure the equality for arbitrary φ_i and curve \mathbf{h} , we only require the equality to hold for a family of simple functions

on simple paths. In practice, we select the pow functions and paths on directly related parameters x'_{i_d} s. Since both sides of Equation (45) are linear functionals of φ_i , equality only needs to hold for the elementary power functions. So we have the following definition.

Definition 5. *If for all polynomial functions $\varphi_n(t)$ of degree n , equality*

$$\int_T \varphi_n(t) \tilde{h}'(t) dt = - \int_T \varphi'_n(t) h(t) dt \quad (44)$$

holds for all $n \leq m$ but not for $n > m$, we say $\tilde{h}'(t)$ estimates the weak derivative $h'(t)$ with a degree of precision of m on path T . If $m \geq 1$, we say the estimation is unbiased.

The definition above quantifies how well the estimation of a weak derivative is. The definition of biasedness conforms to the fact that the derivative is the best local linear approximation. For a multidimensional gradient field approximated by the cumulative product of 1D functions, we have the same result if each function satisfies Definition 5.

It's now easy to derive the unbiasedness constraint of the proposed method. In fact, we have the following result.

Corollary 2. *The synthetic weak derivative $\frac{\partial \tilde{h}_j}{\partial x'_i}$ in Equation (14) is an unbiased estimation of the weak derivative $\frac{\partial h_j}{\partial x'_i}$ on path T if the reconstruction kernel $l(\cdot)$ satisfies*

$$\int_T k(x) dx = \int_T \int_{\mathbb{R}} l(y) k(x - y) dy dx. \quad (45)$$

Corollary 2 provides a minimum requirement for the gradient estimation to be unbiased. However, since the binning function is evaluated on a regular grid, the neighborhood information of h can provide useful information when selecting $l(\cdot)$ instead of a random guess. In many cases, $\phi(\cdot)$ attributes to h_i a similar contribution as h_j if i is in a neighborhood of j , then we have $v_{h_i} \approx v_{h_j}$. In other words, we can assume the underlying cotangent function space to be smooth, such that local information provides enough characterization. One simple assumption is that the underlying space should have a minimum slope, then we drive the linear spline kernel $l(x) = \max(1 - |x|, 0)$, which has a minimum support such that Equation (45) holds for a short path T . In fact, It can be proved that the resulting $(l * k)'(x)$ provides a second-order accurate estimate of the weak derivative $k'(x)$ along any path containing $\text{supp}(k) \cap [-1, 1]$, provided that $k(\cdot)$ is symmetric with respect to some vertical axis. We conduct the following experiments on this linear reconstruction kernel.

A.4 PYTORCH/JAX IMPLEMENTATION OF FBP

This part provides the detailed implementation in PyTorch and JAX for implementing the proposed FBP.

PyTorch (Paszke et al., 2019) is based on reverse-mode automatic differentiation (VJP). A function with custom AD rules should be implemented as a subclass of `torch.autograd.Function` as follows.

Listing 1: PyTorch implementation of FBP as custom VJP rules.

```
import torch

class FunctionalBinning(torch.autograd.Function):
    @staticmethod
    def forward(ctx, xarray, yarray, weights, grid_size):
        ctx.save_for_backward(xarray, yarray, weights)
        # Standard binning with k (Forward pass is unchanged!)
        return k_kernel_binning(xarray, yarray, weights, grid_size)

    @staticmethod
    def backward(ctx, grad_frame):
        xarray, yarray, weights = ctx.saved_tensors
        # Use synthesized transposed derivative with kappa (Eq. 14)
        xarray_dot = kappa_kernel_dx_transposed(\
```

```

    grad_frame, xarray, yarray, grid_size)
yarray_dot = kappa_kernel_dy_transposed(\_
    grad_frame, xarray, yarray, grid_size)
return xarray_dot * weights, yarray_dot * weights, None, None

```

The only extra work to do is to derive the transposed derivative kernel of $\kappa(\cdot)$. JAX (Bradbury et al., 2018) is based on forward-mode automatic differentiation (JVP). A function with custom AD rules should be implemented by decorating it with `custom-jvp` and implementing the custom JVP rules as follows.

Listing 2: JAX implementation of FBP as custom JVP rules.

```

import jax

@jax.custom_jvp
def FunctionalBinning(xarray, yarray, weights, grid_size):
    # Standard binning with k (Forward pass is unchanged!)
    return k_kernel_binning(xarray, yarray, weights, grid_size)

@FunctionalBinning.defjvp
def FunctionalBinning_JVP(primals, tangents):
    xarray, yarray, weights, grid_size = primals
    xarray_dot, yarray_dot, *_ = tangents

    # 1. Run standard forward pass
    frame = FunctionalBinning(xarray, yarray, weights, grid_size)

    # 2. Compute synthesized derivative using kappa (Eq. 14)
    # instead of evaluating Dirac deltas.
    frame_dot = kappa_kernel_dx_binning(\_
        xarray, yarray, xarray_dot * weights, grid_size) + \
        kappa_kernel_dy_binning(\_
            xarray, yarray, yarray_dot * weights, grid_size)

    return frame, frame_dot

```

A.5 EXPERIMENTAL DETAILS

We first provide the exact formula of κ_{rect} , κ_{linear} , and κ_{gauss} , which are used to surrogate the gradient rule of the respective kernels k_{rect} , k_{linear} , and k_{gauss} .

$$\kappa_{rect}(x) = \begin{cases} \frac{3}{4} - x^2, & |x| < \frac{1}{2} \\ \frac{1}{8}(3 - 2|x|)^2, & \frac{1}{2} \leq |x| < \frac{3}{2} \\ 0, & |x| \geq \frac{3}{2} \end{cases} \quad (46)$$

$$\kappa_{linear}(x) = \begin{cases} \frac{1}{6}(4 + 3(-2 + |x|)|x|^2), & |x| < 1 \\ \frac{1}{6}(2 - |x|)^3, & 1 \leq |x| < 2 \\ 0, & |x| \geq 2 \end{cases} \quad (47)$$

$$\kappa_{gauss}(x) = \begin{cases} \frac{1}{2}(x - 1)\text{erf}\left(\frac{x-1}{\sqrt{2}}\right) - x\text{erf}\left(\frac{x}{\sqrt{2}}\right) \\ + \frac{1}{2}(x + 1)\text{erf}\left(\frac{x+1}{\sqrt{2}}\right) + \frac{e^{-\frac{1}{2}(x+1)^2}(e^{2x} - 2e^{x+\frac{1}{2}} + 1)}{\sqrt{2\pi}}, & |x| < \frac{1}{2} \\ \frac{1}{2}\left((|x| - 1)\text{erf}\left(\frac{|x|-1}{\sqrt{2}}\right) - 2x\text{erf}\left(\frac{x}{\sqrt{2}}\right) + \text{erf}\left(\frac{3}{2\sqrt{2}}\right)|x|\right) \\ + \text{erf}\left(\frac{3}{2\sqrt{2}}\right) - 2\sqrt{\frac{2}{\pi}}e^{-\frac{x^2}{2}} + \sqrt{\frac{2}{\pi}}e^{-\frac{1}{2}(|x|-1)^2} + \frac{\sqrt{\frac{2}{\pi}}}{e^{9/8}}, & \frac{1}{2} \leq |x| < \frac{3}{2} \\ \frac{1}{2}(|x| - 1)\text{erf}\left(\frac{x-1}{\sqrt{2}}\right) - \frac{1}{2}\text{erf}\left(\frac{3}{2\sqrt{2}}\right)(|x| - 1) \\ + \frac{e^{-\frac{1}{2}(|x|-1)^2}}{\sqrt{2\pi}} - \frac{1}{e^{9/8}\sqrt{2\pi}}, & \frac{3}{2} \leq |x| < \frac{5}{2} \\ 0, & |x| \geq \frac{5}{2} \end{cases} \quad (48)$$

Although the expressions are definite, they are scaled to match the exact binning function, so they are adaptive to the specific scene.

A.6 ADDITIONAL EXPERIMENTAL RESULTS

Due to space limitations, detailed results for the analysis and applications are presented here. Table 4 and Table 5 provide the optimization results for all the sequences, where our methods are in bold with optimizer L-BFGS-B suffixed by 1 and trust-ncg suffixed by 2. These tables demonstrate another benefit of our method, which is to provide second-order information to facilitate optimization.

Table 4: Angular velocity estimation results. Accuracy in °/s. The optimization time is in milliseconds. n/a means the optimization process has early stops due to abnormal function values.

Score	Methods	boxes		dynamic		poster		shapes	
		acc	time	acc	time	acc	time	acc	time
Var	Rect	44.61	22.42	16.03	23.38	47.09	22.60	44.47	32.34
	FuncRect 1	12.44	6.50	6.67	7.44	14.26	6.55	15.89	10.26
	FuncRect 2	10.91	3.00	6.11	4.24	12.83	3.30	23.94	9.96
	Linear	10.21	6.38	5.63	6.60	12.58	6.36	15.82	9.18
	FuncLinear 1	9.82	5.26	5.53	5.82	12.16	5.39	15.75	9.06
	FuncLinear 2	9.66	2.61	5.50	4.77	12.01	3.19	14.93	13.07
	Gauss 1	10.93	7.14	6.59	8.38	12.51	7.41	14.29	11.13
	Gauss 2	9.61	5.01	6.22	8.36	10.80	5.49	15.79	33.87
	FuncGauss 1	10.27	6.91	6.22	7.98	11.91	7.22	13.81	11.45
	FuncGauss 2	9.95	2.46	5.98	5.59	11.59	3.26	13.85	14.78
LL	Rect	17.47	21.02	8.58	21.50	17.45	20.00	18.62	27.73
	FuncRect 1	10.14	8.07	5.88	9.57	12.42	8.17	14.26	15.18
	FuncRect 2	10.95	4.31	8.48	8.73	13.80	5.67	n/a	n/a
	Linear	9.04	7.29	5.33	8.93	11.53	7.98	13.36	13.30
	FuncLinear 1	8.77	6.74	5.21	7.97	11.30	6.71	13.74	13.72
	FuncLinear 2	8.70	3.29	5.21	7.35	11.22	4.05	14.62	34.21
	Gauss 1	8.99	8.68	5.64	10.28	10.97	8.80	13.46	15.89
	Gauss 2	7.93	5.95	5.36	12.10	9.97	6.85	14.54	57.10
	FuncGauss 1	8.89	8.64	5.49	10.17	10.91	8.59	13.37	16.75
	FuncGauss 2	8.64	3.80	5.35	9.51	10.74	5.30	13.41	29.52

For additional optical flow estimation results, refer to Table 6 and Figure 7. The results are consistent with the main text that our method improves the overall robustness.

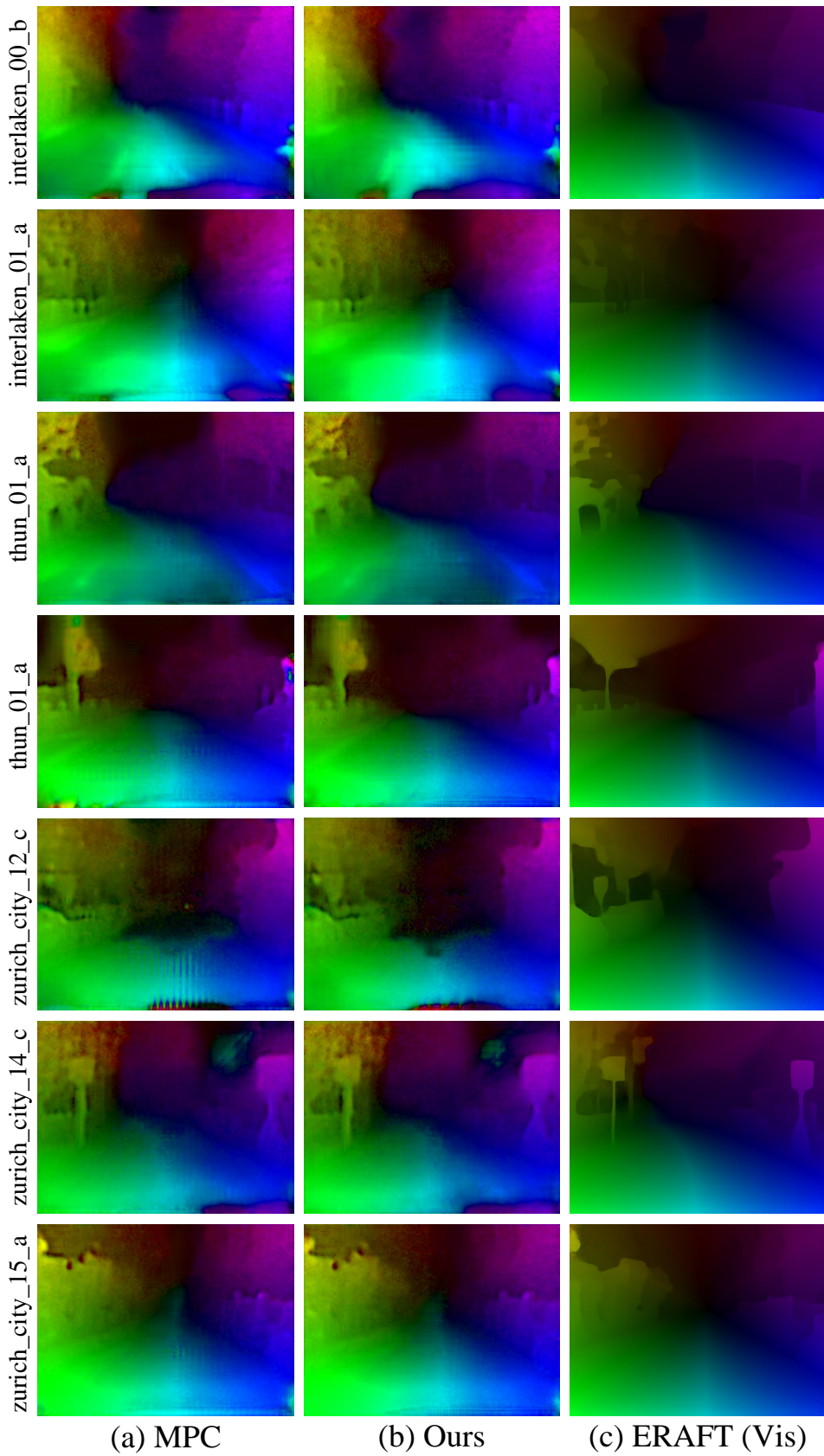


Figure 7: Optical flow estimation results on all 7 test sequences of DSEC (Gehrig et al., 2021a).

Table 5: Linear velocity estimation results. Accuracy in m/s. The optimization time is in milliseconds. n/a means the optimization process has early stops due to abnormal function values.

Score	Methods	boxes		dynamic		poster		shapes	
		acc	time	acc	time	acc	time	acc	time
Var	Rect	0.924	n/a	0.447	n/a	0.326	19.45	0.913	n/a
	FuncRect 1	0.875	n/a	0.209	7.93	0.304	6.45	0.739	n/a
	FuncRect 2	0.679	3.40	0.208	5.18	0.304	3.55	0.257	10.73
	Linear	0.680	6.28	0.208	6.75	0.304	6.22	0.250	8.33
	FuncLinear 1	0.683	5.63	0.208	6.78	0.303	5.64	0.249	8.16
	FuncLinear 2	0.683	3.48	0.208	6.77	0.303	3.71	0.250	12.73
	Gauss 1	1.069	n/a	0.209	8.14	0.803	n/a	0.796	n/a
	Gauss 2	0.689	5.26	0.209	8.67	0.305	5.44	0.249	24.64
	FuncGauss 1	0.688	6.84	0.209	8.81	0.304	7.02	0.248	11.45
	FuncGauss 2	0.689	3.85	0.209	8.38	0.305	4.22	0.249	15.35
LL	Rect	0.763	18.34	0.217	20.05	0.308	18.00	0.258	25.84
	FuncRect 1	0.681	7.97	0.432	n/a	0.303	8.10	0.673	n/a
	FuncRect 2	0.683	6.00	0.218	12.12	0.304	6.28	0.663	n/a
	Linear	0.684	7.91	0.215	10.11	0.304	7.89	0.706	n/a
	FuncLinear 1	0.685	6.96	0.215	9.61	0.304	7.13	0.257	14.01
	FuncLinear 2	0.685	6.00	0.216	11.47	0.304	5.30	0.256	28.93
	Gauss 1	1.108	n/a	0.450	n/a	0.304	8.76	0.861	n/a
	Gauss 2	0.689	7.65	0.217	15.62	0.305	7.99	0.257	50.15
	FuncGauss 1	0.688	8.59	0.218	12.34	0.710	n/a	0.795	n/a
	FuncGauss 2	0.689	6.72	0.218	15.39	0.305	7.24	0.257	31.05

Table 6: Comparison of MPC and MPC (w/ FBP) across multiple sequences. Metrics are End-Point Error (EPE), Angular Error (AE), and percentage of outliers (%Out).

Method	All			interlaken_00_b			interlaken_01_a			thun_01_a		
	EPE	AE	%Out	EPE	AE	%Out	EPE	AE	%Out	EPE	AE	%Out
MPC	2.81	8.96	14.48	3.33	5.11	19.41	2.42	6.17	16.15	1.48	6.70	8.33
MPC (w/ FBP)	2.54	8.33	13.31	3.26	5.05	18.96	2.36	5.70	15.70	1.42	6.39	7.52
Method	thun_01_b			zurich_city_12_a			zurich_city_14_c			zurich_city_15_a		
	EPE	AE	%Out	EPE	AE	%Out	EPE	AE	%Out	EPE	AE	%Out
MPC	1.47	5.88	8.18	5.98	21.56	21.02	1.97	9.74	15.25	1.54	6.71	9.25
MPC (w/ FBP)	1.45	5.64	7.67	4.71	19.65	17.67	1.90	9.22	13.82	1.50	6.22	7.95